Linear and nonlinear optical properties of realistic quantum-wire structures: The dominant role of Coulomb correlation

Fausto Rossi
Istituto Nazionale Fisica della Materia (INFM) and Dipartimento di Fisica, Università di Modena, via Campi 213/A, I-41100 Modena, Italy
and Fachbereich Physik und Zentrum für Materialwissenschaften, Philipps–Universität Marburg, Renthof 5, 35032 Marburg, Germany

Elisa Molinari
Istituto Nazionale Fisica della Materia (INFM) and Dipartimento di Fisica, Università di Modena, via Campi 213/A, I-41100 Modena, Italy
(Received 15 January 1996)

A systematic analysis of the linear and nonlinear optical properties of realistic quantum wires is presented. The proposed theoretical approach, based on a set of generalized semiconductor Bloch equations, provides a full three-dimensional multisubband description of carrier-carrier correlation for any profile of the confinement potential, thus allowing a direct comparison with experiments on available structures. In agreement with previous investigations based on simplified one-dimensional models, our analysis shows that, also for realistic quantum-wire structures, electron-hole Coulomb correlation completely removes the one-dimensional band-edge singularities from the linear-absorption spectra. Moreover, we find that this effect is present also at high densities (corresponding to gain regimes) and contributes significantly in suppressing the ideal sharp features of the free-carrier density of states. The multisubband nature of available state-of-the-art structures is found to play a dominant role in determining the overall spectral shape in the whole density range. [S0163-1829(96)05123-5]

I. INTRODUCTION

One-dimensional (1D) semiconductor structures have received much interest in recent years, and promising advances have been obtained in quantum-wire fabrication and in applications, e.g., to laser devices.[1] The current research aims at achieving structures with improved performance with respect to their three-dimensional (3D) and two-dimensional (2D) counterparts, by taking advantage of the 1D singularities that are expected in the density of states and optical spectra on the basis of single-particle band models.

However, it is now well known that excitonic and correlation effects may be very important in low-dimensional semiconductors.[2,3] For 1D systems, such effects were studied mostly within single-subband one-dimensional models (including electron-hole interaction through modified 1D Coulomb potential).[4,5] Within these models, the band-edge singularity in the 1D density of states (DOS) is smoothed when excitonic effects are taken into account; moreover, Coulomb correlation is found to reduce the absorption spectrum above the band edge, contrary to the well known results for 2D and 3D systems.[4]

The influence of Coulomb correlation on the optical spectra of realistic wires and its implications for device performances has not been fully explored so far. It is, therefore, important to extend the above studies to the wires made available by state-of-the-art technology, which are still far from an ideal 1D nature owing to the size and shape of their confinement potential. Indeed, in *V*-groove[1,6–10] or *T*-shaped cleaved-edge structures,[11] quasi-one-dimensional confinement has been demonstrated for the lowest level,[1,6–8,10,11] while excited states gradually approach a 2D-like behavior. Also, subband separation is still relatively small in all the available samples, so that coupling between different subbands may be important.

The purpose of the present paper is to introduce a theoretical scheme allowing a full three-dimensional treatment of Coulomb correlation in multisubband nanostructures with realistic geometries, in a wide range of temperatures and carrier densities. Our approach is based on a set of generalized semiconductor Bloch equations, which are solved within the Hartree-Fock approximation and provide the modified optical spectrum for bound and continuum states in the linear and nonlinear regimes. Moreover, the calculations allow us to understand the ingredients that are responsible of such modifications.

Within such scheme, we shall address the key issue, whether electron-hole correlation is still expected to heavily affect the optical spectra of quantum wires when their actual size and shape are taken into account. We shall also discuss in which cases its effects may hinder the possible advantages of the reduced dimensionality in the intervals of temperature and carrier density, which may be relevant for device applications. Apart from its relevance in terms of basic many-body Coulomb theory, the answer to these questions is important for the perspectives of quantum-wire physics and technology.

The paper is organized as follows. In Sec. II, we describe the proposed theoretical approach, we introduce the physical system as well as the kinetic equations, and discuss the in-

gredients and the typical quantities obtained as an output of the calculations. Section III presents our numerical results for a typical V-shaped quantum wire: In Sec. III A the single-particle results are presented, while in Sec. III B the various many-body effects induced by Coulomb correlation are discussed both in the linear and nonlinear regimes. Finally, in Sec. IV we discuss the implications of our results and draw some conclusions.

II. THEORETICAL APPROACH

The physical system under investigation is a gas of carriers confined in a quasi-one-dimensional semiconductor structure. As usual, the total Hamiltonian of the system can be regarded as the sum of two terms: A term describing the single-particle properties, i.e., free carriers plus confinement potential plus carrier-light interaction, and a term describing many-body effects, i.e., Coulomb correlation. As usual, the latter will be treated within some approximation scheme.

A. Single-particle description

Let us consider the gas of noninteracting carriers, electrons (e) and holes (h) confined within the quasi-one-dimensional semiconductor structure. The quantum confinement is described in terms of a potential $V_c^{e/h}$, the height of which is dictated by the conduction-valence-band discontinuities.

Since the energy region of interest is relatively close to the wire band gap, we describe the bulk band structure in terms of the usual effective-mass approximation. In addition, since the confinement potential $V_c^{e/h}$ is a slowly varying function on the scale of the lattice periodicity, we work within the ''envelope-function approximation.''

By denoting with z the free wire direction, the confinement potential $V_c^{e/h}$ is a function of the two confinement directions x and y only; Therefore, the system is still translationally invariant along the wire direction and the z component of the carrier wave vector k_z is a ''good'' quantum number. As a consequence, the carrier wave function can be factorized in terms of a plane wave along the free direction, z, times an envelope function $\phi(x,y)$ over the normal plane; the carriers within our wire structure are then described by the following 2D Schrödinger equation:

$$\left[-\frac{\hbar^2}{2m^{e/h}}\left(\frac{\partial^2}{\partial^2 x}+\frac{\partial^2}{\partial^2 y}\right)+V_c^{e/h}(x,y)\right]\phi_\nu^{e/h}(x,y) = \epsilon_\nu^{e/h}\phi_\nu^{e/h}(x,y), \tag{1}$$

where $m^{e/h}$ denotes the bulk effective mass for electrons or holes. Here, the set of eigenvalues $\epsilon_\nu^{e/h}$ corresponds to the energy levels of the carriers induced by the confinement-potential profile $V_c^{e/h}$; therefore, the explicit form of the band structure for a carrier in the wire is

$$\epsilon_{k_z\nu}^{e/h}=\epsilon_\nu^{e/h}+\frac{\hbar^2 k_z^2}{2m^{e/h}}. \tag{2}$$

For each of the energy levels $\epsilon_\nu^{e/h}$, we thus have a 1D parabolic band, named ''subband'' and characterized by the same bulk effective mass $m^{e/h}$.

For the ideal case of rectangular wires with infinite potential barriers, the problem can be again factorized along the two confinement directions x and y.[12] On the contrary, for the case of V-shaped,[1,6–8,10] or T-shaped structures,[11] we are forced to consider a truly two-dimensional approach. Our numerical solution of the 2D Schrödinger equation (1), which is based on a plane-wave expansion with periodic boundary conditions, is described in Appendix A. Such a numerical approach can be easily generalized to the case of an applied magnetic field as described in Ref. 13.

In terms of the above single-particle representation $\{k_z\nu\}$ [i.e., the set of 3D eigenfunctions $\Phi_{k_z\nu}^{e/h}(\mathbf{r}) \propto \phi_\nu^{e/h}(x,y)e^{ik_z z}$ and the corresponding band structure $\epsilon_{k_z\nu}^{e/h}$], the single-particle Hamiltonian, i.e., the Hamiltonian describing the free carriers within our 1D structure interacting with a classical light field, can be written as

$$\begin{aligned}\mathbf{H}^{\mathrm{sp}}=&\sum_{k_z\nu_e}\epsilon_{k_z\nu_e}^{e}c_{k_z\nu_e}^{\dagger}c_{k_z\nu_e}+\sum_{k_z\nu_h}\epsilon_{k_z\nu_h}^{h}d_{k_z\nu_h}^{\dagger}d_{k_z\nu_h}\\&-\sum_{k_z,\nu_e\nu_h}[M_{k_z,\nu_e\nu_h}E_0(t)e^{-i\omega_L t}c_{k_z\nu_e}^{\dagger}d_{-k_z\nu_h}^{\dagger}\\&+M_{k_z,\nu_h\nu_e}E_0^{*}(t)e^{i\omega_L t}d_{-k_z\nu_h}c_{k_z\nu_e}],\end{aligned} \tag{3}$$

where the second-quantization operators $c_{k_z\nu_e}^{\dagger}$ ($d_{k_z\nu_h}^{\dagger}$) and $c_{k_z\nu_e}$ ($d_{k_z\nu_h}$) describe, respectively, the creation and the annihilation of an electron (a hole) in state $k_z\nu_e$ ($k_z\nu_h$). Here,

$$M_{k_z,\nu_e\nu_h}=M_{k_z}^{\mathrm{bulk}}\int dx\,dy\,\phi_{\nu_e}^{e*}(x,y)\phi_{\nu_h}^{h}(x,y) \tag{4}$$

denotes the dipole matrix element for the optical transition $k_z\nu_h\rightarrow k_z\nu_e$, while $E_0(t)$ is the amplitude of the external light field with frequency ω_L. The carrier-light interaction is treated within the usual dipole and rotating-wave approximations.

B. Many-body description

The carriers within the quantum wire interact via the Coulomb potential $V^0(\mathbf{r})$. Due to such interaction, several correlation effects take place. Here, only processes conserving the total number of carriers are considered, thus Auger recombination and impact ionization are neglected. Such processes are known to become important only at very high densities and at energies high up in the band.[14]

The many-body Hamiltonian describing carrier-carrier interaction within our $k_z\nu$ representation is given by

$$\begin{aligned}\mathbf{H}^{\mathrm{mb}}=&\sum_{k_z^1\nu_e^1,k_z^2\nu_e^2,k_z^3\nu_e^3,k_z^4\nu_e^4}\frac{1}{2}V^0_{k_z^1\nu_e^1,k_z^2\nu_e^2;k_z^3\nu_e^3,k_z^4\nu_e^4}\\&\times c^{\dagger}_{k_z^1\nu_e^1}c^{\dagger}_{k_z^2\nu_e^2}c_{k_z^3\nu_e^3}c_{k_z^4\nu_e^4}\\&+\sum_{k_z^1\nu_h^1,k_z^2\nu_h^2,k_z^3\nu_h^3,k_z^4\nu_h^4}\frac{1}{2}V^0_{k_z^1\nu_h^1,k_z^2\nu_h^2;k_z^3\nu_h^3,k_z^4\nu_h^4}\\&\times d^{\dagger}_{k_z^1\nu_h^1}d^{\dagger}_{k_z^2\nu_h^2}d_{k_z^3\nu_h^3}d_{k_z^4\nu_h^4}\end{aligned}$$

$$-\sum_{k_z^1\nu_e^1,k_z^2\nu_h^2,k_z^3\nu_h^3,k_z^4\nu_e^4} V^0_{k_z^1\nu_e^1,k_z^2\nu_h^2;k_z^3\nu_h^3,k_z^4\nu_e^4} \times c^\dagger_{k_z^1\nu_e^1} d^\dagger_{-k_z^2\nu_h^2} d_{-k_z^3\nu_h^3} c_{k_z^4\nu_e^4}, \quad (5)$$

where

$$V^0_{k_z^1\nu^1,k_z^2\nu^2;k_z^3\nu^3,k_z^4\nu^4} = \int d\mathbf{r} \int d\mathbf{r}'\, \Phi^{e/h*}_{k_z^1\nu^1}(\mathbf{r}) \Phi^{e/h*}_{k_z^2\nu^2}(\mathbf{r}') \times V^0(\mathbf{r}-\mathbf{r}') \Phi^{e/h}_{k_z^3\nu^3}(\mathbf{r}') \Phi^{e/h}_{k_z^4\nu^4}(\mathbf{r}) \quad (6)$$

are the matrix elements of the ''bare'' Coulomb potential $V^0(\mathbf{r})$ for the generic two-particle transition $k_z^4\nu^4, k_z^3\nu^3 \rightarrow k_z^1\nu^1, k_z^2\nu^2$. We want to stress the full 3D nature of the present approach based on the knowledge of the 3D carrier wave functions Φ. The explicit evaluation of the above matrix elements for a generic 2D confinement-potential profile $V_c^{e/h}$, i.e., for a generic set of wave functions $\phi^{e/h}_{k_z\nu}$, is described in Appendix B.

The first two terms on the right-hand side of Eq. (5) describe the repulsive electron-electron and hole-hole interactions, while the third one describes the attractive interaction between electrons and holes. Due to the multisubband nature of our approach, all these three terms describe intrasubband, as well as intersubband interaction processes.[12]

The presence of free carriers leads to a two-component screening of the Coulomb potential V^0. As usual, the screened potential V can be schematically written as

$$V = \varepsilon^{-1} V^0, \quad (7)$$

where ε^{-1} denotes the inverse of the dielectric tensor ε. As for any confined system, we deal with a nondiagonal dielectric tensor. It is not the aim of the present paper to discuss the derivation of the dielectric response of a multisubband 1D system. We will employ the multisubband screening model discussed in Ref. 12.

C. Kinetic equations

Starting from the above $\{k_z\nu_{e/h}\}$ representation, we introduce the following kinetic description: We consider as kinetic variables the various distribution functions of electrons and holes (intraband density-matrix elements),

$$f^e_{k_z\nu_e} = \langle c^\dagger_{k_z\nu_e} c_{k_z\nu_e} \rangle, \quad f^h_{k_z\nu_h} = \langle d^\dagger_{k_z\nu_h} d_{k_z\nu_h} \rangle, \quad (8)$$

as well as the corresponding diagonal ($\nu_e = \nu_h = \nu$) polarization fields (interband density-matrix elements),

$$p_{k_z\nu} = \langle d_{-k_z\nu} c_{k_z\nu} \rangle. \quad (9)$$

Such polarizations $p_{k_z\nu}$ describe the phase coherence between electrons in state $k_z\nu_e$ and holes in state $-k_z\nu_h$; Therefore, they reflect the degree of coherence of our electron-hole system and, more precisely, they are proportional to the 3D exciton wave function in our $k_z\nu$ representation:

$$\psi(\mathbf{r}_e, \mathbf{r}_h) \propto \sum_{k_z\nu} p_{k_z\nu} \Phi^e_{k_z\nu}(\mathbf{r}_e) \Phi^{h*}_{k_z\nu}(\mathbf{r}_h). \quad (10)$$

In particular, starting from the above exciton wave function ψ, we can define a 1D electron-hole correlation function vs the relative free coordinate $z = z^e - z^h$ as

$$g(z) \propto \sum_{k_z k_z'\nu} p^*_{k_z\nu} p_{k_z'\nu} e^{i(k_z' - k_z)z}. \quad (11)$$

The kinetic description introduced in Eqs. (8) and (9) is a generalization to 1D systems of a standard approach for the study of bulk semiconductors[3,15] recently applied also to quantum well structures[16] and superlattices.[17]

The time evolution of the above kinetic variables is obtained by applying the standard ''Heisenberg-equation technique'' as described in Refs. 3,15. The total Hamiltonian $\mathbf{H} = \mathbf{H}^{\rm sp} + \mathbf{H}^{\rm mb}$, the explicit form of which is given in Eqs. (3) and (5), induces two different contributions to the dynamics of the system:

$$\frac{\partial}{\partial t} f^{e/h}_{k_z\nu} = \frac{\partial}{\partial t} f^{e/h}_{k_z\nu}\Big|_{\rm sp} + \frac{\partial}{\partial t} f^{e/h}_{k_z\nu}\Big|_{\rm mb},$$

$$\frac{\partial}{\partial t} p_{k_z\nu} = \frac{\partial}{\partial t} p_{k_z\nu}\Big|_{\rm sp} + \frac{\partial}{\partial t} p_{k_z\nu}\Big|_{\rm mb}. \quad (12)$$

The single-particle Hamiltonian $\mathbf{H}^{\rm sp}$ in Eq. (3) leads to the following set of kinetic equations:

$$\frac{\partial}{\partial t} f^{e/h}_{\pm k_z\nu}\Big|_{\rm sp} = \frac{1}{i\hbar}(U_{k_z\nu} p^*_{k_z\nu} - U^*_{k_z\nu} p_{k_z\nu}),$$

$$\frac{\partial}{\partial t} p_{k_z\nu}\Big|_{\rm sp} = \frac{1}{i\hbar}(\epsilon^e_{k_z\nu} + \epsilon^h_{-k_z\nu}) p_{k_z\nu} + \frac{1}{i\hbar} U_{k_z\nu}(1 - f^e_{k_z\nu} - f^h_{-k_z\nu}), \quad (13)$$

where

$$U_{k_z\nu} = -M_{k_z\nu} E(t) = -M_{k_z\nu} E_0(t) e^{-i\omega_L t} \quad (14)$$

is the unperturbed Rabi energy (proportional to the applied external field through the optical matrix element). Here, the compact notation $M_{k_z\nu} \equiv M_{k_z,\nu\nu}$ has been introduced. The $\pm$ sign in Eq. (13) refers to electrons (e) and holes (h), respectively.

The single-particle dynamics is modified by the many-body Hamiltonian $\mathbf{H}^{\rm mb}$ of Eq. (5). The lowest-order contributions of carrier-carrier interaction, i.e., Hartree-Fock terms, result in a renormalization ΔU (called internal field) of the Rabi energy U, as well as a renormalization $\Delta\epsilon$ of the carrier band structure ϵ:

$$\Delta U_{k_z\nu} = -\sum_{k_z'\nu'} V^{eh}_{k_z\nu,-k_z'\nu';-k_z\nu,k_z'\nu'} p_{k_z'\nu'};$$

$$\Delta\epsilon^{e/h}_{k_z\nu} = -\sum_{k_z'\nu'} V^{ee/hh}_{k_z\nu,k_z'\nu';k_z\nu,k_z'\nu'} f^{e/h}_{k_z'\nu'}. \quad (15)$$

Here, V^{eh} and $V^{ee/hh}$ denote the matrix elements of the screened Coulomb potential introduced in Eq. (7) for the electron-hole and for the electron-electron/hole-hole interaction, respectively. As we can see, the repulsive electron-

electron (*ee*) and hole-hole (*hh*) interactions lead to a renormalization of the corresponding bands, while the attractive electron-hole (*eh*) interaction gives rise to an internal field that is responsible for excitonic effects. Higher-order contributions in $\mathbf{H}^{\mathrm{mb}}$ give rise to carrier-carrier scattering processes,[12] which lead to energy relaxation and dephasing. Such incoherent carrier-carrier contributions, as well as the corresponding carrier-phonon ones, are expected to play a minor role for most of the physical conditions studied in this paper and, therefore, they will not be treated explicitly.

Within the above approximation scheme, the full set of kinetic equations (12) is then given by

$$\frac{\partial}{\partial t} f^{e/h}_{\pm k_z \nu} = \frac{1}{i\hbar}(\mathcal{U}_{k_z \nu} p^*_{k_z \nu} - \mathcal{U}^*_{k_z \nu} p_{k_z \nu}),$$

$$\frac{\partial}{\partial t} p_{k_z \nu} = \frac{1}{i\hbar}(\mathcal{E}^e_{k_z \nu} + \mathcal{E}^h_{-k_z \nu}) p_{k_z \nu} + \frac{1}{i\hbar}\mathcal{U}_{k_z \nu}(1 - f^e_{k_z \nu} - f^h_{-k_z \nu}), \tag{16}$$

where $\mathcal{U} = U + \Delta U$ and $\mathcal{E} = \epsilon + \Delta\epsilon$ denote, respectively, the renormalized Rabi energies and subbands. The above set of kinetic equations can be regarded as a generalization to multisubband 1D systems of the well known semiconductor Bloch equations (SBE) commonly used for the analysis of coherent phenomena in bulk semiconductors.[3,15]

D. Quasiequilibrium optical absorption

In this paper, we focus on the quasiequilibrium regime, i.e., we assume that the carrier system is not driven out of equilibrium by the optical excitation. Therefore, Fermi-Dirac $f^{e/h}_{k_z \nu}$ are assumed and the solution of the set of SBE (16) simply reduces to the solution of the polarization equation

$$\frac{\partial}{\partial t} p_{k_z \nu} = \frac{1}{i\hbar}(\mathcal{E}^e_{k_z \nu} + \mathcal{E}^h_{-k_z \nu}) p_{k_z \nu} + \frac{1}{i\hbar}\mathcal{U}_{k_z \nu}(1 - \tilde{f}^e_{k_z \nu} - \tilde{f}^h_{-k_z \nu}), \tag{17}$$

where $\tilde{f}$ denotes the Fermi-Dirac distribution function. This is now a linear equation in $p_{k_z \nu}$, the general solution of which can be written in terms of its Green's propagator, i.e., the solution corresponding to a δ-like laser excitation $E_0(t) \propto \delta(t)$. The above polarization equation can be solved in two different ways: (i) Within the so called dynamical approach,[15,17,18] the full time evolution of the polarization is obtained by means of a time-step solution of Eq. (17); (ii) The second approach consists in finding the stationary solutions of Eq. (17), i.e., polarization eigenvalues and eigenvectors. In this paper, we employ this last approach, the technical details of which are described in Appendix C.

In order to obtain the optical-absorption spectrum, the total (or macroscopic) polarization

$$P(t) = \frac{1}{\Omega} \sum_{k_z \nu} M^*_{k_z \nu} p_{k_z \nu}(t) \tag{18}$$

is then considered. From its Fourier transform

$$P(\omega) = \int_{-\infty}^{\infty} dt\, e^{i\omega t} P(t), \tag{19}$$

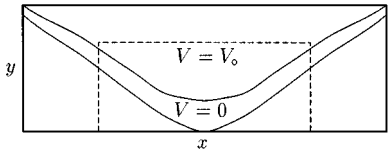

FIG. 1. Typical cross section of *V*-grooved wires derived from TEM micrographs and used to define the confinement potential $V_c^{e/h}(x,y)$ entering the single-particle Schrödinger equation. The frame of the figure (about 130×40 nm) delimits the 2D periodic cell used in the calculation. The dashed lines identify the smaller rectangular region (about 70×25 nm), where single-particle and excitonic wave functions will be plotted (see Figs. 3, 4, and 6 below). The wire width along *y* at the apex of the *V* is about 10 nm.

we derive the optical susceptibility

$$\chi(\omega) = \frac{P(\omega)}{E(\omega)}, \tag{20}$$

where

$$E(\omega) = \int_{-\infty}^{\infty} dt\, e^{i\omega t} E(t) = \int_{-\infty}^{\infty} dt\, e^{i(\omega - \omega_L)t} E_0(t) \tag{21}$$

is the Fourier transform of the external laser field.

The optical susceptibility $\chi(\omega)$ is a complex function; it provides the absorption spectrum as well as the refractive-index change. In particular, the desired absorption spectrum is proportional to its imaginary part:

$$\alpha(\omega) \propto \mathrm{Im}[\chi(\omega)]. \tag{22}$$

We want to stress that within this approach both quantities, i.e., refractive index and absorption spectrum, are independently obtained with no need of applying a Kramers-Kronig transformation.[19]

As discussed above, we solve the polarization equation (17) by numerically computing its stationary solutions, i.e., polarization eigenvalues and eigenvectors. As described in Appendix C, these two ingredients allow us to obtain directly the optical susceptibility $\chi(\omega)$ (and, therefore, the absorption spectrum) avoiding any time-dependent analysis.

III. NUMERICAL RESULTS

In the following, we apply the above theoretical approach to a realistic wire geometry. We consider structures obtained by molecular beam epitaxy overgrowth over *V*-grooved substrates.[8] The typical 2D confinement-potential profile (Fig. 1) is defined according to the wire cross section as derived from TEM micrographs. The thickness of the *V*-shaped region at the apex of the *V* is about 10 nm. The large rectangle in Fig. 1 (about 130×40 nm) delimits the periodicity region used in our calculation. The single-particle wave functions discussed below will instead be plotted in the smaller rectangular portion delimited by dashed lines (about 70×25 nm).

All the results shown in the following refer to typical GaAs-based *V* wires with $Al_xGa_{1-x}As$ barriers; the $Al_xGa_{1-x}As$ composition and all the material parameters are the same as those considered in Ref. 8: $m^e = 0.067 m_0$, $m^h = 0.34 m_0$; $V_c^e = 150$ meV, $V_c^h = 50$ meV.

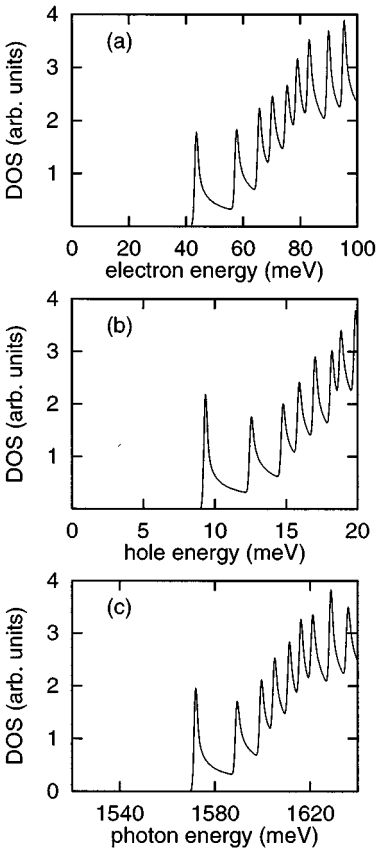

FIG. 2. Single-particle densities of states (a) for electrons and (b) for holes vs excess energies, with respect to the bottom of the bulk bands; (c) corresponding joint density of states vs optical-transition energy.

A. Single-particle analysis

The single-particle energy levels for the various wire subbands, as well as their wave functions, are obtained from a numerical solution of the 2D Schrödinger equation,[8] as described in Sec. II A. The results are shown in Fig. 2 in the form of single-particle DOS for electrons [Fig. 2(a)] and holes [Fig. 2(b)]. Note the different horizontal scales, which represent excess energies with respect to the bottom of their bulk bands. Figure 2(c) reports the corresponding joint DOS as a function of the optical-transition energy.

Figures 3 and 4 show the charge-density contour plots for electrons and holes in their lowest subbands. Here, the stronger hole confinement is apparent and, more important, we notice an increasing charge delocalization with increasing subband index.

We want to stress that, in the present implementation of our method, all the results for holes have been obtained neglecting valence-band mixing (VBM). While recent calculations, performed for wires with rectangular section of comparable size, clearly indicate that VBM should not be important for the lowest confined states,[20] it is known that it may affect the higher-index eigenstates and the corresponding wave functions (hence the selection rules).[21,20] We are currently improving our computational scheme to include VBM, in order to allow a more detailed comparison with experiments in that range. The single-particle states discussed above will be used as basic ingredients for the many-body analysis presented in the following section.

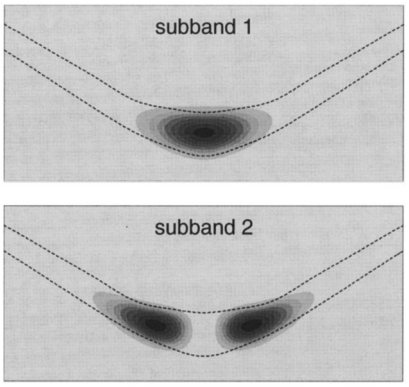

FIG. 3. Single-particle charge-density contour plots $|\phi^e_\nu(x,y)|^2$ for electrons in their first two subbands, $\nu=1$ and $\nu=2$. The plotted region is about 70×25 nm (see also Fig. 1).

B. Many-body analysis

1. Linear response: excitonic regime

We now discuss the results for absorption spectra in the linear regime, as obtained according to Sec. II B. The role played by electron-hole correlation is illustrated in Fig. 5 by comparing results that include Coulomb correlation (CC) with those of the free-carrier (FC) model (solid and dashed lines, respectively). All the spectra have been obtained assuming a Gaussian energy broadening of 2 meV. This relatively small broadening (as compared to that of realistic wire structures[9]) allows a better identification of the effects of electron-hole correlation.

Let us focus first on Fig. 5(a) [Fig. 5(b)], where only the first (second) wire subband is included. It appears that electron-hole correlation gives rise to two major effects: (i) the excitonic peak arises below the onset of the continuum, with a binding energy E_b of about 12 meV for the lowest subband and of about 9 meV for the second one. The difference in E_b reflects the different wave function delocalization along the V sidewalls (see Figs. 3 and 4), as will be discussed with more detail below. These excitonic splittings are in excellent agreement with recent magnetoluminescence

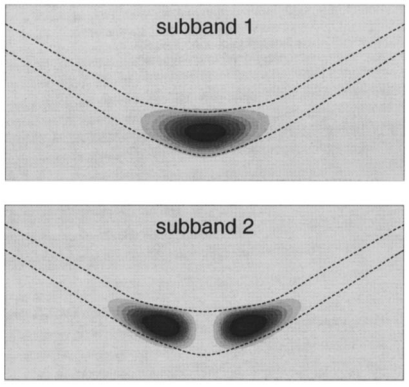

FIG. 4. Single-particle charge-density contour plots $|\phi^h_\nu(x,y)|^2$ for holes in their first two subbands, $\nu=1$ and $\nu=2$. The plotted region is about 70×25 nm (see also Fig. 1).

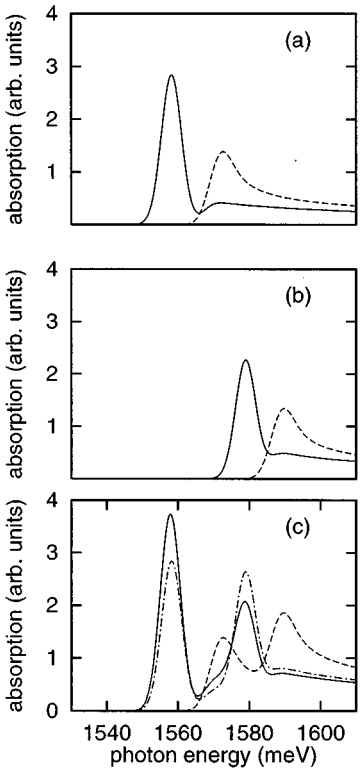

FIG. 5. Absorption spectra of the *V*-shaped wire obtained by including electron-hole Coulomb correlation (CC model, solid line) or by assuming free carriers (FC model, dashed line). (a) Only first subband included; (b) only second subband included; (c) both the two lowest subbands are taken into account. For comparison, the algebraic sum of the CC curves of (a) and (b) (i.e., coupling-free case) is reported in (c) by dash-dotted lines. All spectra were computed assuming a Gaussian energy broadening of 2 meV.

experiments.[8] (ii) The shape of the CC spectrum in the continuum region is drastically modified with respect to the FC one. In agreement with previous investigations based on simplified 1D models,[4,5] we find a strong suppression of the 1D DOS singularity.

Figure 5(c) shows spectra obtained by including both (first and second) subbands. Due to the relatively small intersubband splitting, a significant intersubband coupling is expected. To clarify this effect, in addition to the full CC and FC results, we also report by dash-dotted line the coupling-free CC result [i.e., the algebraic sum of the CC spectra of Figs. 5(a) and 5(b)]. The main manifestation of the intersubband coupling is an oscillator-strength transfer toward the low-energy region, which results in a significant increase of the first exciton peak and a corresponding decrease of the second one.

Let us now focus on the excitonic part of the spectrum and, in particular, let us examine the properties of our quasi-one-dimensional exciton. In order to derive quantitative information on the spatial extension of the various excitons (corresponding to the different wire subbands), we start by considering their wave function $\psi(\mathbf{r}_e,\mathbf{r}_h)$ introduced in Eq. (10). This is in general a function of six coordinates: $\mathbf{r}_e=(x_e,y_e,z_e)$ and $\mathbf{r}_h=(x_h,y_h,z_h)$. Through translational invariance along the free wire direction, these reduce to five coordinates, which can be conveniently chosen as

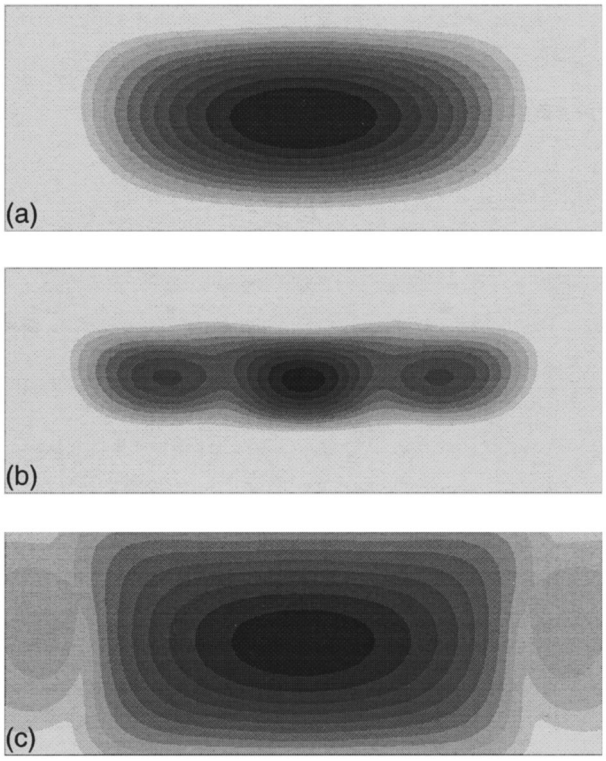

FIG. 6. Correlation function $c(x,y)$ of the ground-state exciton obtained taking into account (a) the first subband only, (b) the second subband only, and (c) both (first plus second) subbands. The plotted region is about 70×25 nm and the origin ($x=x_e-x_h=0$, $y=y_e-y_h=0$) is located at the center of the rectangle. A log scale has been used and all panels are rescaled to the same maximum value.

$x=x_e-x_h$, $X=(x_e+x_h)/2$, $y=y_e-y_h$, $Y=(y_e+y_h)/2$, and $z=z_e-z_h$. By taking $z=0$ and averaging the square of the exciton wave function ψ over the ''macroscopic coordinates'' X and Y, we define an effective exciton correlation function $c(x,y)$ as

$$c(x,y)=\int dX\,dY\,|\psi(x,X;y,Y;z=0)|^2. \tag{23}$$

Figures 6(a) and 6(b) show such correlation function $c(x,y)$ (logarithmic scale) obtained by taking into account, respectively, the first and the second subband only. Note that by definition, $c(x,y)$ is always nonzero and large at the origin (self-correlation point: $r_e-r_h=0$). Moreover, depending on the symmetry and on the degree of localization of the single-particle wave functions entering Eq. (10), it may exhibit additional maxima; This is the case of Fig. 6(b), where the two lateral peaks reflect the correlation between the maxima of the single-particle wave functions localized on the wire ''wings'' (see Figs. 3 and 4). In Fig. 6(c), we also show how the ground-state exciton of Fig. 6(a) is modified when the lowest two subbands are both taken into account: The modified symmetry, due to intersubband coupling, leading to the presence of additional lateral maxima, is clearly visible. On the contrary, due to the different logarithmic scales used in these plots, we are not able to appreciate the increase in the spatial extension of the second exciton [case (b)], with respect to the first one [case (a)].

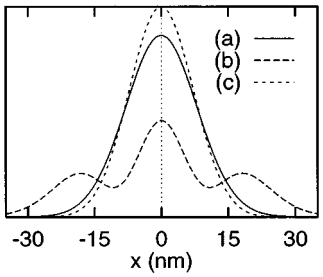

FIG. 7. $y=0$ cross sections of the three correlation functions $c(x,y)$ of Fig. 6: (a) first subband only; (b) second subband only; (c) both (first plus second) subbands.

In order to obtain a more quantitative comparison, in Fig. 7 we plot the $y=0$ cross sections of the three correlation functions of Fig. 6. Now we clearly see an increase of the spatial extension of the second-subband exciton [case (b)] compared to the first-subband one [case (a)]. Moreover, the intersubband coupling in (c) leads to a spatial localization of the ground-state exciton with respect to case (a). This is responsible for the enhanced oscillator strength of the corresponding first exciton peak in Fig. 5(c), with respect to Fig. 5(a).

Let us now focus on the continuum region of the absorption spectra and, in particular, on the dramatic suppression of the band-edge singularity in the CC results of Fig. 5. From Eq. (C21), the absorption coefficient is proportional to the product of the oscillator strength (OS) times the corresponding excitonic DOS ρ of Eq. (C20): We, therefore, study these two quantities separately. In Fig. 8, we compare the DOS ρ obtained within the CC and the FC models (solid and dashed lines, respectively): The difference is hardly visible and the pronounced peak in the DOS (broadened 1D singularity) is not reduced by electron-hole correlation. Figure 9(a) shows that the quantity, which is mainly modified by CC, is the OS. Here, the ratio between the CC and FC OS is plotted as a function of excess energy with respect to the band edge (solid line). In agreement with previous results for simplified 1D models,[4] such a ratio is always smaller than 1 and vanishes at the band edge. Such vanishing behavior is found to dominate the 1D DOS singularity and, as a result, the absorption spectrum at the band edge exhibits the regular behavior of Fig. 5(a) (solid line). The dashed line in Fig. 9(a)

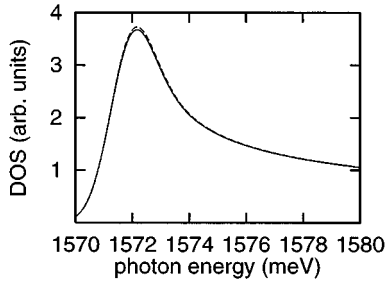

FIG. 8. Electron-hole DOS ρ of the *V*-shaped wire close to the band edge, obtained within the CC (solid line) and FC model (dashed line). Both curves were computed assuming a Gaussian energy broadening of 0.2 meV. The difference is hardly visible on this scale (see text).

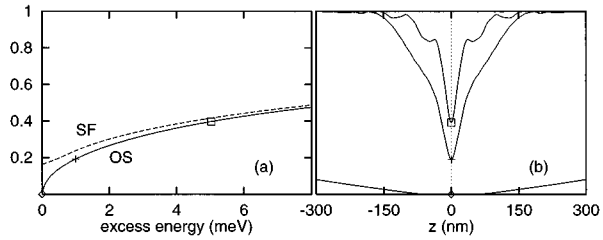

FIG. 9. (a) Solid line: ratio between CC and FC oscillator strength (OS); dashed line: ratio between the CC and FC absorption spectra (Sommerfeld factor, SF), as a function of the excess energy close to the band edge. (b) Electron-hole correlation function $g(z)$ vs relative distance $z=z^e-z^h$ for three different values of the excess energy, identified by the corresponding symbols in (a). $g(z=0)$ is the probability of finding the electron and hole at the same place and gives directly the oscillator strength for the corresponding excess energy.

is the resulting ratio between the CC and FC absorption, commonly named Sommerfeld factor (SF). As a consequence of the OS behavior, the SF turns out to be less than unity over this energy region.

This behavior is opposite to the known results for 2D and 3D cases, where a SF value greater than unity has been usually ascribed to the attractive electron-hole interaction. It is, therefore, interesting to elucidate the origin of such behavior in our case. To this purpose, we recall that for the case of a single subband the oscillator strength of Eq. (C23) coincides with the value at $z=0$ of the correlation function $g(z)$ defined in Eq. (11), i.e., the probability of finding the electron and hole at the same place (corresponding to the square of the exciton wave function in a 1D model[4]).

In Fig. 9(b), we plot $g(z)$ for three different values of the excess energy. Note that its values at $z=0$ correspond to the values of the OS ratio at the same energies [Fig. 9(a) solid line]. Moreover, an ''electron-hole correlation hole'' is clearly visible, the spatial extension of which strongly increases when approaching the band edge. Therefore, our analysis of the electron-hole correlation function $g(z)$ confirms that the vanishing behavior of the OS in Fig. 9(a) reflects a sort of electron-hole ''effective repulsion.''

To summarize this section, we can conclude that also for our realistic quantum-wire geometries electron-hole correlation leads to a strong suppression of the 1D band-edge singularity in the linear-absorption spectrum. This is definitely due to the strong reduction of oscillator strength which, in turn, originates from an ''effective electron-hole repulsion'' typical of 1D systems.

2. Nonlinear response: gain regime

The results discussed so far were all obtained within the linear-response regime, i.e., in the limit of very low carrier densities. However, most of the potential quantum-wire applications, i.e., 1D lasers and modulators, operate in strongly nonlinear regimes.[1] In general, for such conditions additional aspects become important: screening effects, band renormalization, and phase-space filling. Since all these effects are already accounted for in the formulation of our generalized SBE (Sec. II B), our approach can be directly applied also to

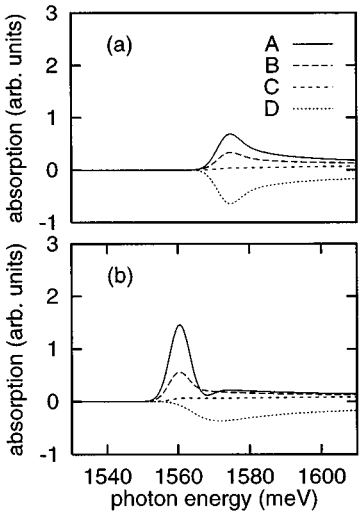

FIG. 10. Nonlinear absorption spectra of the *V*-shaped wire at room temperature calculated including only the lowest wire subband for increasing carrier densities: *A*: $n=10^4$ cm^{-1}; *B*: $n=5\times10^5$ cm^{-1}; *C*: $n=10^6$ cm^{-1}; *D*: $n=4\times10^6$ cm^{-1}. (a) Free-carrier model, and (b) Coulomb-correlated model. In case *D*, the system is already in the gain regime.

the high-carrier-density regime. We believe this is an important advantage of the present theoretical approach.

In the following, we show the first quantitative analysis of nonlinear absorption spectra of realistic *V*-shaped wire structures for different carrier densities at room temperature. The screening model used in the calculation is described in Ref. 12.

Once more, we start by analyzing the simplified case of a single subband: In Fig. 10, only the lowest wire subband is included [as in Fig. 5(a)]; The free-carrier [Fig. 10(a)] and Coulomb-correlated spectra [Fig. 10(b)] are separately shown for different carrier densities.

In the CC case, we clearly recognize the exciton peak in the low-density limit (case *A*: $n=10^4$ cm^{-1}). With increasing carrier density, the strength of the excitonic absorption decreases, due to phase-space filling and screening of the attractive electron-hole interaction, and moreover the band renormalization leads to a redshift of the continuum. Above the Mott density (here about 8×10^5 cm^{-1}), the exciton completely disappears. At a density of 4×10^6 cm^{-1} (case *D*) the spectrum already exhibits a negative region corresponding to stimulated emission, i.e., the gain regime.

As for the case of the linear-response regime, let us discuss first the excitonic properties. Figure 11 shows the correlation function $g(z)$ corresponding to the ground-state exciton for the four densities of Fig. 10. In the low-density limit (case *A*, solid line), we see the typical correlation function of an attractive electron-hole pair in its ground state. With increasing carrier density, we approach the Mott transition: After an initial delocalization, which reflects the electron-electron and hole-hole screening of the attractive electron-hole interaction (case *B*), the ground-state exciton level enters the continuum and the electron-hole localization around $z=0$ tends to vanish (case *C*). This is due, in addition to the screening, also to the Pauli factor $(1-\tilde{f}^e-\tilde{f}^h)$ in Eq. (C6), which for such carrier density tends to vanish. A

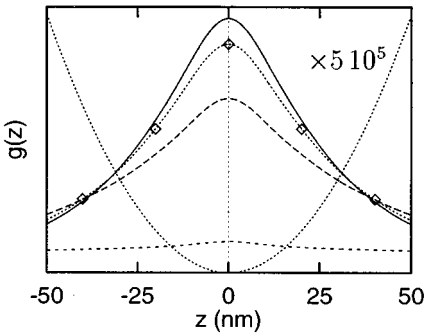

FIG. 11. Electron-hole correlation function $g(z)$ of the ground-state exciton at densities corresponding to the CC spectra of Fig. 10(b). For the case *D* (gain regime), the result obtained neglecting the Pauli factor in Eq. (C6) is also shown (curve marked with diamonds, see text).

further increase in the density leads to the gain regime: The Pauli factor becomes negative and, as a consequence, the attractive electron-hole interaction transforms into a repulsive one. In such conditions we have a fully continuum energy spectrum, the ground state of which is characterized by a very small oscillator strength. The corresponding correlation function (case *D* without diamonds) shows a typical repulsion hole around $z=0$, where its value is strongly reduced with respect to that of *A*, *B*, and *C* (note that curve *D* has been magnified by a factor 5×10^5 in Fig. 11). In order to better understand the role played by the Pauli factor, we have also reported in Fig. 11 the result *D* obtained neglecting the Pauli factor (curve marked with diamonds). In this case, the electron-hole interaction is screened but still attractive, thus resulting in a correlation function $g(z)$ similar to that of cases *A*–*C*.

Let us now focus on the continuum region of the spectra in Fig. 10(b). By comparison with Fig. 10(a), we notice that the typical shape of the band-edge singularity in the ideal FC gain spectrum is strongly modified by electron-hole correlation. The reason is again understood by analyzing the Pauli-free oscillator strength (PFOS) (Ref. 22) plotted in Fig. 12(a) for the same carrier densities of Fig. 10(a) together with the

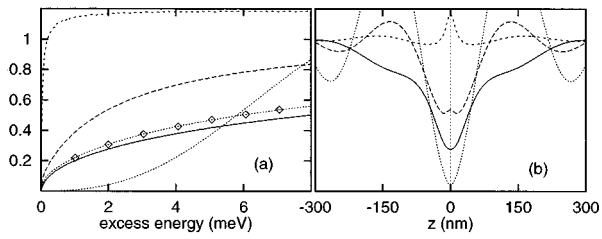

FIG. 12. (a) Ratio between CC and FC Pauli-free oscillator strength (PFOS) (Ref. 22) corresponding to the absorption spectra of Fig. 10. Here, for the case *D* (gain regime), the result obtained neglecting the Pauli factor in Eq. (C6) (curve marked with diamonds) is also shown (see text). (b) Electron-hole correlation functions $g(z)$ corresponding to the CC spectra of Fig. 10(b) for an excess energy of 2 meV. Again, $g(z=0)$ is the probability of finding the electron and hole at the same place and reflects the Pauli-free oscillator strength corresponding to this excess energy [see Fig. 12(a)].

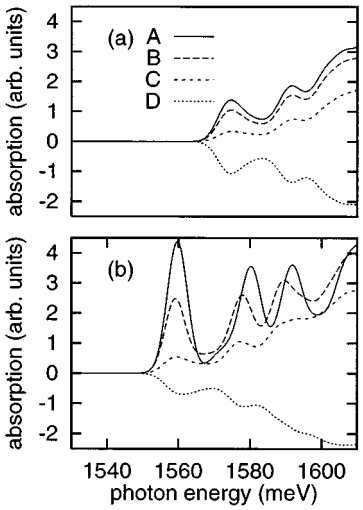

FIG. 13. Nonlinear absorption spectra of the *V*-shaped wire at room temperature calculated including the lowest 12 subbands for increasing carrier densities: *A*: $n=10^4$ cm^{-1}; *B*: $n=10^6$ cm^{-1}; *C*: $n=4\times10^6$ cm^{-1}; *D*: $n=2\times10^7$ cm^{-1}. (a) Free-carrier model, and (b) Coulomb-correlated model.

corresponding correlation functions $g(z)$ reported in Fig. 12(b). Also, for relatively high carrier densities (cases *C* and *D*), the OS corresponding to the CC model goes to zero at the band edge as previously seen in the low-density limit [Fig. 9(a)]. As a consequence, the FC peak is strongly suppressed and only its high-energy tail survives. The overall result is a broader and less pronounced gain region in the CC case as compared with the FC one.

From a detailed analysis of Fig. 12(a), we see a qualitatively different behavior of the OS in the gain regime (case *D*) as compared to the low-density result (case *A*). By considering the corresponding result obtained neglecting the Pauli factor (curve marked with diamonds), we clearly see that this transition in the OS shape is mainly ascribed to the attractive $\rightarrow$ repulsive transition induced by the Pauli factor. This is also confirmed from the corresponding correlation functions $g(z)$ reported in Fig. 12(b). As for the linear-absorption regime [Fig. 9(b)], the correlation functions (all corresponding to an excess energy of 2 meV) exhibit a sort of ''hole'' around $z=0$. This is well extended in the low-density limit (case *A*), it decreases with increasing carrier densities (cases *B* and *C*), and, finally, in the gain regime (case *D*) it is again well pronounced reflecting the attractive nature of the electron-hole interaction induced by the Pauli factor in Eq. (C6).

Our analysis of the CC spectra seems also to indicate a small redshift of the band gap with increasing carrier density, as previously found for the case of 3D and 2D systems.[3,23] However, we consider this result very preliminary: a more refined screening model (including nondiagonal terms of the dielectric tensor[12]) is required to confirm it and to provide a more detailed analysis of band-gap renormalization.

Finally, Fig. 13 shows the full nonlinear spectra for our realistic *V*-shaped wire, with the 12 lowest subbands included. For the present wire geometry, the multisubband nature is found to play an important role in modifying the typical shape of the gain spectra, which for both the FC [Fig. 13(a)] and the CC model [Fig. 13(b)] extend over a much larger range than in the single-subband case (Fig. 10). The intersubband-coupling effects and the Coulomb-induced suppression of the 1D singularities both contribute together to the smearing of the structures in the high-carrier-density absorption spectra and in the gain profile.

Our analysis indicates that, for the typical structure considered here (where we have assumed negligible disorder and scattering-induced broadening), the shape of the absorption spectra over the whole density range greatly differs from the sharp 1D spectrum predicted by any free-carrier model.

IV. SUMMARY AND CONCLUSIONS

We have presented a theoretical analysis of the linear and nonlinear optical properties of realistic quantum wires. Our approach is based on a numerical solution of the semiconductor Bloch equations describing the multisubband 1D system. In spite of its accuracy, the method is very flexible and allows us to study realistic wires of arbitrary geometry. We have applied such approach to a typical *V*-shaped structure, the parameters of which reflect the current state-of-the-art in the quantum-wire fabrication.

The role of electron-hole Coulomb correlation has been discussed by a systematic comparison with the corresponding free-carrier spectra at various carrier concentrations. In addition to the strong excitonic features typical of the low-density limit, we have found, in general, a suppression of the 1D band-edge singularities, which has been ascribed to a strong reduction of oscillator strength, originating in turn from an ''effective electron-hole repulsion'' typical of 1D quantum confinement.

In the high-density regime, the realistic multisubband wire spectrum shows an extended gain region with relatively broad structures. By comparing the nonlinear multisubband absorption spectra with ideal single-subband spectra, we can conclude that the large gain region is mainly due to the small intersubband splitting compared to the single-subband gain range. This confirms that, in order to obtain sharp gain profiles, one of the basic steps in quantum-wire technology is to produce structures with increased subband splitting.

Finally, we notice that the disorder-induced inhomogeneous broadening, not considered here, is known to increase significantly the spectral broadening[9] and this effect is expected to increase with increasing subband splitting. Therefore, small but extremely high-quality structures (i.e., single-monolayer control) seem to be the only possible candidates for successful quantum-wire applications.

ACKNOWLEDGMENTS

We thank R. Cingolani, R. Enderlein, T. Meier, M. Pascoli, R. Rinaldi, L. Rota, and P.E. Selbmann for stimulating and fruitful discussions. This work was supported in part by the EC Commission through the ESPRIT NANOPT project and the Network ''ULTRAFAST.''

APPENDIX A: SOLUTION OF THE 2D SCHRÖDINGER EQUATION

Let us consider the set of basis wave functions

$$\phi^0_{n_x n_y}(x,y)=\frac{1}{\sqrt{L_x L_y}}e^{i(k_x x+k_y y)}, \tag{A1}$$

with $k_x=2\pi n_x/L_x$, $k_y=2\pi n_y/L_y$. Here, L_x and L_y denote, respectively, the x and y size of the 2D periodicity box. The solution of the 2D Schrödinger equation (1) can be expanded in terms of such plane-wave representation as

$$\phi(x,y)=\sum_l c_l\phi_l^0(x,y), \tag{A2}$$

where the compact notation $l\equiv k_xk_y$ has been introduced. As a consequence, Eq. (1) is transformed into the eigenvalue problem:

$$\sum_{l'}(H_{ll'}-\epsilon\delta_{ll'})c_{l'}=0, \tag{A3}$$

with

$$H_{ll'}=T_l\delta_{ll'}+\int_\Omega dx\,dy\;\phi_l^{0*}(x,y)V_c^{e/h}(x,y)\phi_{l'}^0(x,y). \tag{A4}$$

Here, $\Omega=L_xL_y$ denotes the 2D volume, while $T_l=\hbar^2(k_x^2+k_y^2)/(2m^{e/h})$ is the kinetic energy corresponding to the plane-wave state l. The carrier energy levels, i.e., the eigenvalues ϵ and the corresponding eigenfunctions (in terms of the eigenvectors c_l) are obtained by direct diagonalization of the single-particle Hamiltonian matrix $H_{ll'}$. This approach can be easily generalized to the case of an applied magnetic field as described in Ref. 13.

For the V-shaped wires considered in this paper, we have used a set of about 2000 plane waves within a periodicity box of about 130×40 nm (see Fig. 1). This allows us to obtain, with high accuracy (better than 1%), the first twelve electron and hole energy levels (see Fig. 2) used as ingredients for the solution of the SBE. However, for a detailed analysis of high-energy states (close to the 3D continuum), convergence problems may arise for two reasons: first, the number of plane waves could be inadequate, and second, a fictitious interwire coupling due to the finite dimensions of our periodicity box may play some role. By increasing the number of plane waves and the size of the box, we have checked that this is definitely not the case for the ''close-to-gap'' energy region discussed in this paper.

APPENDIX B: EVALUATION OF THE COULOMB MATRIX ELEMENTS

In order to evaluate the Coulomb matrix elements introduced in Eq. (6), we start by replacing the potential V^0 by its 3D Fourier expansion:

$$V^0(\mathbf{r})=\sum_{\mathbf{q}}\widetilde{V}_{\mathbf{q}}e^{i\mathbf{q}\cdot\mathbf{r}}. \tag{B1}$$

After this substitution, we obtain

$$\begin{aligned}V^0_{k_z^1\nu^1,k_z^2\nu^2;k_z^3\nu^3,k_z^4\nu^4}&=\sum_{\mathbf{q}}\widetilde{V}_{\mathbf{q}}\int d\mathbf{r}\int d\mathbf{r}'\,\Phi^{e/h*}_{k_z^1\nu^1}(\mathbf{r})\Phi^{e/h*}_{k_z^2\nu^2}\\&\quad\times(\mathbf{r}')e^{i\mathbf{q}\cdot(\mathbf{r}-\mathbf{r}')}\Phi^{e/h}_{k_z^3\nu^3}(\mathbf{r}')\Phi^{e/h}_{k_z^4\nu^4}(\mathbf{r})\\&=\sum_{\mathbf{q}}\widetilde{V}_{\mathbf{q}}\int d\mathbf{r}\,\Phi^{e/h*}_{k_z^1\nu^1}(\mathbf{r})e^{i\mathbf{q}\cdot\mathbf{r}}\Phi^{e/h}_{k_z^4\nu^4}(\mathbf{r})\\&\quad\times\int d\mathbf{r}'\,\Phi^{e/h*}_{k_z^2\nu^2}(\mathbf{r}')e^{-i\mathbf{q}\cdot\mathbf{r}'}\Phi^{e/h}_{k_z^3\nu^3}(\mathbf{r}').\end{aligned} \tag{B2}$$

This leads to a factorization of the two space coordinates $\mathbf{r}$ and $\mathbf{r}'$, therefore suggesting the introduction of the following form factors:

$$F_{k_z\nu,k_z'\nu';\mathbf{q}}=\int d\mathbf{r}\,\Phi^{e/h*}_{k_z\nu}(\mathbf{r})e^{i\mathbf{q}\cdot\mathbf{r}}\Phi^{e/h}_{k_z'\nu'}(\mathbf{r}). \tag{B3}$$

In terms of these form factors, the Coulomb matrix elements can be simply written as

$$V^0_{k_z^1\nu^1,k_z^2\nu^2;k_z^3\nu^3,k_z^4\nu^4}=\sum_{\mathbf{q}}\widetilde{V}_{\mathbf{q}}F_{k_z^1\nu^1,k_z^4\nu^4;\mathbf{q}}F^*_{k_z^3\nu^3,k_z^2\nu^2;\mathbf{q}}. \tag{B4}$$

Therefore, the evaluation of the Coulomb matrix elements in Eq. (6) reduces to the evaluation of the form factors F in Eq. (B3).

If we now insert into Eq. (B3) the factorized form of the wave functions

$$\Phi^{e/h}_{k_z\nu}(\mathbf{r})=\phi^{e/h}_\nu(x,y)\frac{1}{\sqrt{L_z}}e^{ik_zz}, \tag{B5}$$

we obtain

$$\begin{aligned}F_{k_z\nu,k_z'\nu';\mathbf{q}}&=\int dx\,dy\;\phi^{e/h*}_\nu(x,y)e^{i(q_xx+q_yy)}\phi^{e/h}_{\nu'}(x,y)\frac{1}{L_z}\\&\quad\times\int dz\,e^{i(k_z'-k_z+q_z)z}\\&=\int dx\,dy\;\phi^{e/h*}_\nu(x,y)e^{i(q_xx+q_yy)}\phi^{e/h}_{\nu'}(x,y)\\&\quad\times\delta(k_z'-k_z+q_z).\end{aligned} \tag{B6}$$

The remaining 2D integral over the xy plane can be easily rewritten in terms of the plane-wave representation discussed in Appendix A. More specifically, by replacing the 2D eigenfunctions with their plane-wave expansion given in Eq. (A2) and using the orthonormality of the plane waves over the 2D periodicity region, we obtain

$$\begin{aligned}F_{k_z\nu,k_z'\nu';\mathbf{q}}&=\delta(k_z'-k_z+q_z)\sum_{n_xn_y,n_x',n_y'}c^*_{n_xn_y}c_{n_x',n_y'}\\&\quad\times\delta(k_x'-k_x+q_x)\,\delta(k_y'-k_y+q_y).\end{aligned} \tag{B7}$$

Therefore, for any shape of the confinement potential, starting from the numerically computed eigenvectors $c_{n_xn_y}$, we are able to obtain the various form factors F which, in turn, allow us to numerically compute the desired Coulomb matrix elements.

APPENDIX C: SOLUTION OF THE POLARIZATION EQUATION

As discussed in Sec. II D, the polarization equation (17) is solved within the so-called stationary approach, i.e., by computing polarization eigenvalues and eigenvectors. This consists in finding solutions of the form

$$p_{k_z\nu}(t)=p_{k_z\nu}e^{-i(\mathcal{E}t/\hbar)}. \tag{C1}$$

By inserting this stationary solution into Eq. (17) together with the explicit form (15) of the internal field ΔU and by treating the external-field term U as a source term, the corresponding homogeneous equation can be rewritten as

$$(\mathcal{E}^e_{k_z\nu}+\mathcal{E}^h_{-k_z\nu}-\mathcal{E})p_{k_z\nu}-(1-\tilde{f}^e_{k_z\nu}-\tilde{f}^h_{-k_z\nu})$$

$$\times\sum_{k_z'\nu'} V^{\mathrm{eh}}_{k_z\nu,k_z'\nu';k_z\nu,k_z'\nu'}p_{k_z'\nu'}=0. \tag{C2}$$

By introducing again the compact notation $l\equiv k_z\nu$, the above equation can be easily transformed into the following eigenvalue problem:

$$\sum_{l'}(S_{ll'}-\mathcal{E}\delta_{ll'})p_{l'}=0, \tag{C3}$$

with

$$S_{ll'}=T_l\delta_{ll'}-W_{ll'}. \tag{C4}$$

Here,

$$T_l=T_{k_z\nu}=\mathcal{E}^e_{k_z\nu}+\mathcal{E}^h_{-k_z\nu} \tag{C5}$$

denotes the renormalized optical-transition energy, while

$$W_{ll'}=W_{k_z\nu,k_z'\nu'}=(1-\tilde{f}^e_{k_z\nu}-\tilde{f}^h_{-k_z\nu})V^{\mathrm{eh}}_{k_z\nu,k_z'\nu';k_z\nu,k_z'\nu'} \tag{C6}$$

is the screened electron-hole Coulomb matrix element weighted by the corresponding Pauli factor.

From a direct diagonalization of the matrix S, we obtain a set of polarization eigenvalues $\mathcal{E}^\lambda$ and eigenvectors p^λ. As discussed in Sec. II C, the microscopic polarization $P_{k_z\nu}$ is directly related to the excitonic wave function ψ [see Eq. (10)]. Therefore, the diagonalization of the matrix S provides all the excitonic properties of the system: The set of eigenvalues $\mathcal{E}^\lambda$ gives the energy spectrum that reflects all the excitonic properties of the quantum-wire structure, e.g., the exciton binding energies and the DOS of the continuum. For each energy level $\mathcal{E}^\lambda$ of the interacting electron-hole system (i.e., for each exciton eigenstate), the knowledge of the corresponding eigenvector p^λ allows us to compute its exciton wave function ψ according to Eq. (10). Moreover, the various elements p^λ_l of a given eigenvector p^λ, being the components of a given exciton eigenstate λ in the basis of the free-particle states l, correspond to the scalar product between excitonic and free-particle states:

$$p^\lambda_l=\langle l|\lambda\rangle,\quad p^{\lambda *}_l=\langle\lambda|l\rangle. \tag{C7}$$

Therefore, they are the matrix elements of the unitary transformation, which connects the excitonic to the free electron-hole picture.

Finally, let us evaluate within our stationary approach the optical susceptibility $\chi(\omega)$ introduced in Eq. (20). Due to the linearity of the polarization equation (17), the optical susceptibility, being its Green's propagator, is independent of the particular choice of the external field $E_0(t)$. Therefore, we are allowed to consider as a laser field the convenient δ-like laser excitation,

$$E_0(t)=\tilde{E}\,\delta(t), \tag{C8}$$

characterized by a constant (frequency-independent) Fourier transform,

$$E(\omega)=\tilde{E}. \tag{C9}$$

With this particular choice of the external laser field, the polarization equation (17) can be written as

$$\frac{\partial p_l}{\partial t}=\frac{1}{i\hbar}\sum_{l'}S_{ll'}p_{l'}+\frac{i\tilde{E}}{\hbar}\tilde{M}_l\delta(t), \tag{C10}$$

where

$$\tilde{M}_l=\tilde{M}_{k_z\nu}=M_{k_z,\nu\nu}(1-\tilde{f}^e_{k_z\nu}-\tilde{f}^h_{-k_z\nu}) \tag{C11}$$

is the optical matrix element weighted by the corresponding Pauli factor. If we now apply to Eq. (C10) the unitary transformation $l\rightarrow\lambda$ (free carriers $\rightarrow$ excitons) given in Eq. (C7), we obtain

$$\frac{\partial p^\lambda}{\partial t}=\frac{\mathcal{E}^\lambda}{i\hbar}p^\lambda+\frac{i\tilde{E}}{\hbar}\tilde{M}^\lambda\delta(t), \tag{C12}$$

with

$$\tilde{M}^\lambda=\sum_l p^{\lambda *}_l\tilde{M}_l. \tag{C13}$$

The solution of this equation is simply given by

$$p^\lambda(t)=\frac{i\tilde{E}}{i\hbar}\tilde{M}^\lambda e^{-i\mathcal{E}^\lambda t/\hbar}. \tag{C14}$$

Starting from the above result, we can now evaluate within our excitonic picture λ the total polarization introduced in Eq. (18):

$$P(t)=\frac{1}{\Omega}\sum_l M^*_l p_l(t)=\frac{1}{\Omega}\sum_\lambda M^{\lambda *}p^\lambda(t)$$

$$=\frac{i\tilde{E}}{\hbar\Omega}\sum_\lambda M^{\lambda *}\tilde{M}^\lambda e^{-i\mathcal{E}^\lambda t/\hbar}, \tag{C15}$$

where

$$M^\lambda=\sum_l p^{\lambda *}_l M_l \tag{C16}$$

denotes the optical matrix element within our λ representation.

The final step in the derivation of the optical susceptibility χ consists in evaluating the Fourier transform (19) of the total polarization:

$$P(\omega)=\int_{-\infty}^{\infty} dt\, e^{i\omega t}P(t)=\frac{2\pi i\widetilde{E}}{\Omega}\sum_{\lambda} M^{\lambda *}\widetilde{M}^{\lambda}\delta(\hbar\omega-\mathcal{E}^{\lambda}). \tag{C17}$$

The optical susceptibility is then given by

$$\chi(\omega)=\frac{2\pi i}{\Omega}\sum_{\lambda} M^{\lambda *}\widetilde{M}^{\lambda}\delta(\hbar\omega-\mathcal{E}^{\lambda}). \tag{C18}$$

As discussed in Sec. II D, the absorption spectrum $\alpha(\omega)$ is proportional to the imaginary part of the optical susceptibility and, in our case, is given by

$$\alpha(\omega)\propto \mathrm{Im}[\chi(\omega)]\propto\sum_{\lambda} \mathrm{Re}[M^{\lambda *}\widetilde{M}^{\lambda}]\delta(\hbar\omega-\mathcal{E}^{\lambda}). \tag{C19}$$

If we now consider that the quantity

$$\rho(\hbar\omega)=\sum_{\lambda} \delta(\hbar\omega-\mathcal{E}^{\lambda}) \tag{C20}$$

is just the excitonic density of states at energy $\hbar\omega$, we can finally write the absorption spectrum as

$$\alpha(\hbar\omega)\propto a(\hbar\omega)\rho(\hbar\omega), \tag{C21}$$

where the OS

$$a(\hbar\omega)=\langle \mathrm{Re}[M^{\lambda *}\widetilde{M}^{\lambda}]\rangle_{\mathcal{E}^{\lambda}=\hbar\omega} \tag{C22}$$

has been introduced. This is defined as the average value of the quantity $\mathrm{Re}[M^{\lambda *}\widetilde{M}^{\lambda}]$ over all the states λ with energy $\hbar\omega$. From Eq. (C21), we see that the absorption spectrum can be always regarded as the product of the oscillator strength a times the corresponding excitonic DOS ρ.

In the low-density limit (linear-response regime), the Pauli factor in Eq. (C11) is equal to unity, $\widetilde{M}^{\lambda}$ reduces to M^{λ}, and the oscillator strength is given by

$$a^{\mathrm{lr}}(\hbar\omega)=\langle |M^{\lambda}|^2\rangle_{\mathcal{E}^{\lambda}=\hbar\omega}. \tag{C23}$$

Moreover, for the case of a single-subband system, it can be easily shown that the above oscillator-strength coincides with the value of the correlation function g introduced in Eq. (11) for $z=0$, a well known result for the case of simplified 1D systems.[4]

As a final remark, we want to stress that within the proposed approach the quantities a and ρ from which the absorption spectrum originates can be directly computed from the knowledge of the polarization eigenvalues $\mathcal{E}^{\lambda}$ and eigenvectors p^{λ}, thus avoiding any time-dependent analysis.

[1] For a review, see R. Cingolani and R. Rinaldi, Riv. Nuovo Cimento **16**, 1 (1993).

[2] See, e.g., Proceedings of the 3rd International Conference on Optics of Excitons in Confined Systems, edited by G. Bastard and B. Gil [J. Phys. (France) IV **C3**, 5 (1993)]; see, also, Proceedings of the 4th International Conference on Optics of Excitons in Confined Systems, edited by F. Bassani, G. C. La Rocca, and A. Qualtropani [Nuovo Cimento D **17** (1995)].

[3] H. Haug and S.W. Koch, *Quantum Theory of the Optical and Electronic Properties of Semiconductors*, 3rd ed. (World Scientific, Singapore, 1994).

[4] Tetsuo Ogawa and Toshihide Takagahara, Phys. Rev. B **43**, 14 325 (1991); **44**, 8138 (1991).

[5] S. Benner and H. Haug, Phys. Rev. B **47**, 15 750 (1993).

[6] E. Kapon *et al.*, Phys. Rev. Lett. **63**, 430 (1989); M. Grundmann *et al.*, J. Nonlin. Opt. Phys. Mater. **4**, 99 (1995).

[7] M. Gailhanou *et al.*, Appl. Phys. Lett. **62**, 1623 (1993).

[8] R. Rinaldi *et al.*, Phys. Rev. Lett. **73**, 2899 (1994).

[9] E. Molinari *et al.*, in *Proceedings of the 22nd International Conference on the Physics of Semiconductors*, edited by D.J. Lockwood (World Scientific, Singapore, 1994), p. 1707.

[10] S. Tiwari *et al.*, Appl. Phys. Lett. **64**, 3536 (1994).

[11] L. Pfeiffer *et al.*, Appl. Phys. Lett. **56**, 967 (1990); W. Wegscheider *et al.*, *ibid*. **65**, 2510 (1994).

[12] L. Rota *et al.*, Phys. Rev. B **52**, 18 319 (1995).

[13] F. Rossi, E. Molinari, R. Rinaldi, and R. Cingolani, Proceedings of the 7th International Conference on Modulated Semiconductor Structures (MSS-7), Madrid, 1995 [Solid-State Electron. (to be published)]; R. Rinaldi *et al.* (unpublished).

[14] W. Quade, E. Schöll, F. Rossi, and C. Jacoboni, Phys. Rev. B **50**, 7398 (1994).

[15] T. Kuhn and F. Rossi, Phys. Rev. Lett. **69**, 977 (1992); Phys. Rev. B **46**, 7496 (1992).

[16] E. Binder, T. Kuhn, and G. Mahler, Phys. Rev. B **50**, 18 319 (1994).

[17] T. Meier, F. Rossi, P. Thomas, and S.W. Koch, Phys. Rev. Lett. **75**, 2558 (1995).

[18] K.-C. Je, T. Meier, F. Rossi, and S.W. Koch, Appl. Phys. Lett. **67**, 2978 (1995).

[19] See, also, D.S. Citrin and Y.-C. Chang, IEEE J. Quantum Electron. **QE-29**, 97 (1993), where, however, excitonic effects are neglected.

[20] G. Goldoni and A. Fasolino, Phys. Rev. B **52**, 14 118 (1995).

[21] U. Bockelmann and G. Bastard, Phys. Rev. B **45**, 1688 (1992).

[22] With Pauli-free oscillator strength, we refer to the oscillator strength given in Eq. (C23), i.e., that obtained by neglecting the Pauli factor in Eq. (C11): $\widetilde{M}^{\lambda}\rightarrow M^{\lambda}$. This quantity, which is always positive-definite, differs from the oscillator strength in Eq. (C22). However, as for the linear-response regime, it reflects the value of the correlation function $g(z)$ at any carrier density [see Eq. (11)].

[23] See, e.g., R. Cingolani and K. Ploog, Adv. Phys. **40**, 535 (1991); R. Cingolani *et al.*, Phys. Rev. B **48**, 14 331 (1993), and references therein.